Article:
Bailey, D.J., Lawson, S.M., Sun, S.K. et al. (2020) A new approach to the immobilisation of technetium and transuranics: Co-disposal in a zirconolite ceramic matrix. Journal of Nuclear Materials, 528. 151885. ISSN: 0022-3115

https://doi.org/10.1016/j.jnucmat.2019.151885

A new approach to the immobilisation of technetium and transuranics: co-disposal in a zirconolite ceramic matrix

D. J. Bailey[1], S. M. Lawson[1], S. K. Sun[1], M. C. Stennett[1], T-H. Lee[1,2], B.Ravel[3], C. L. Corkhill[1], J. Heo[2] & N. C. Hyatt[1]

1- Immobilisation Science Laboratory, Department of Materials Science and Engineering, University of Sheffield, United Kingdom.

2- Department of Materials Science and Engineering and Division of Advanced Nuclear Engineering, Pohang University of Science and Technology (POSTECH), Pohang, Gyeongbuk, 37673, Republic of Korea.

3- National Institute of Standards and Technology, 100 Bureau Drive, Gaithersburg MD 20899, USA.

Abstract

Technetium and transuranic elements (TRUs) are long-lived radionuclides, produced as a result of nuclear power generation. Co-immobilisation of these radionuclides in a ceramic wasteform is attractive as they are problematic for vitrification and would reduce the demand on a future geological disposal facility. A range of zirconolite ceramics have been produced *via* an oxide route using the surrogates Mo and Ce with a view to the co-immobilisation of Tc and TRUs. The resultant materials were characterised by XRD, SEM-EDX, TEM and XAS. Final phase assemblage was found to be affected by target stoichiometry, the Ca precursor used, processing temperature and processing atmosphere. Through appropriate optimisation of processing conditions and target stoichiometry, the results of this study show co-immobilisation of Tc and TRUs is a promising approach.

Introduction

Civil nuclear programmes lead to the production of significant amounts of transuranic elements (TRUs), such as plutonium and americium, and technetium. The long-lived radiotoxicity of both TRUs and technetium (^{239}Pu $t_{1/2}$ = 24,000 years, ^{241}Am $t_{1/2}$ = 432 years, ^{237}Np $t_{1/2}$ = 2,100,000 years, ^{99}Tc $t_{1/2}$ = 211,000 years) necessitates their isolation from the biosphere, typically by disposal in a GDF. Prior to GDF disposal, radionuclides must be immobilised in a

suitable host matrix such as a glass or ceramic. The limited solubility of technetium and TRUs in borosilicate glasses makes vitrification a less attractive option for immobilisation [1]. It is possible to extract Tc and TRUs during high level waste reprocessing by the use of further solvent extraction stages in a modification of the PUREX process. In the proposed UREX process, Tc is co-extracted with U and later separated, TRUs may be extracted later in the process *via* the TALSPEAK or other process [2]. Consequently, separated waste streams are possible and immobilisation in a ceramic wasteform, where higher waste loadings may be possible, is attractive. However, routing technetium and TRUs for disposal in separate streams would require the development of two distinct wasteforms and increase the demands placed on a geological disposal facility. For these reasons, the prospect of co-immobilisation of both TRUs and Tc in a robust host matrix is an attractive concept.

A proposed ceramic wasteform for the disposal of plutonium, that may be extended to incorporate other transuranic elements, is zirconolite, $CaZrTi_2O_7$ [3–5]. Zirconolite is the target actinide bearing component of Synroc formulations and has previously been synthesised *via* both alkoxide and oxide routes [6–8]. The zirconolite structure is a derivative of the pyrochlore structure and comprises alternating layers of TiO_6 octahedra in a hexagonal tungsten bronze array (HTB) and Zr and Ca in seven and eight-fold coordination, respectively [9,10]. Ti is situated in three separate sites; two fully occupied octahedral sites and a half-occupied trigonal bi-pyramidal site. There are several known polytypes of zirconolite including monoclinic, trigonal and orthorhombic symmetries (2M, 4M, 3T, 6T and 3O) [11,12]. The various polytypes arise due to differences in the stacking order of the TiO_6 layers, cation site substitution, synthesis conditions, including oxygen fugacity, and temperature [4,9,12].

Natural zirconolite samples have been found to accommodate and retain actinides despite metamictisation and several previous studies have investigated the incorporation and retention of actinides (U, Np, Pu, Cm) in synthetic zirconolites [3,4,13–15]. Laboratory studies of synthetic zirconolites have found zirconolite to be highly corrosion resistant in a range of media (acidic and basic) at temperatures up to 250 ºC with enhanced dissolution and formation of alteration phases observed at T > 250 ºC [16,17]. Pu has previously been shown to readily substitute into the zirconolite structure with the site occupied dependent on Pu valence, processing conditions and the designed stoichiometry [13].

Tc has previously been successfully incorporated into the zirconolite-related pyrochlore structure in the Tc (IV) oxidation state [18]. The $4d^3$ electron configuration of Tc (IV) suggests

a strong preference for octahedral co-ordination in oxides (associated with crystal field stabilisation energy) and the ionic radius of Tc (IV) is similar to Ti (IV) (0.785 cf. 0.745 Å); it should therefore be feasible to substitute Tc for Ti in $CaZrTi_2O_7$ [19]. The relatively low volatilisation temperature of Tc_2O_7 (311 °C [1]) complicates the processing of Tc bearing ceramics, redox control must be maintained to ensure retention of the more thermally stable TcO_2 (slight volatility above 900 ºC, no decomposition up to 1100 °C [20]). Samples of technetate pyrochlores (Tc (IV)) have previously been successfully produced by high temperature treatment of oxide precursors under vacuum [20,21].

This study was conceived to investigate the possibility of co-immobilisation of TRUs and Tc in a zirconolite matrix by synthesising zirconolites in the $Ca_{1-x/2}Zr_{1-x/2}Ce_xTi_{2-x}Mo_xO_{7\pm\delta}$ series (x = 0.1, 0.2, 0.3) using Ce (III/IV) and Mo (IV) as structural analogues for TRU (III/IV) and Tc (IV), respectively (relative ionic radii 0.79 cf. 0.785 Å for Tc (IV)/Mo (IV) and 1.01 cf. 1.0 Å for Ce (IV)/Pu (IV)). Zirconolites were formulated with the intention of Ce (III/IV) substitution on both the Ca and Zr sites, respectively; this solid solution mechanism has been characterised for Pu in previous investigations [13].

Experimental

Zirconolites were prepared by solid state reaction between ZrO_2, $CaCO_3$, MoO_2, CeO_2 and TiO_2 precursors. Precursors were mixed with isopropanol to form a slurry and milled using a Fritsch Pulverisette 6 for five periods of three minutes at 500 rpm, reversing the direction of milling with each period. The milled slurry was dried overnight and sintered pellets were produced by uniaxially pressing batched powders in a hardened steel die (10 mm diameter) and sintering under atmosphere (argon or 5% H_2/N_2) for 12 hours at temperatures of 1200, 1250, 1300, 1350 and 1400 ºC. Hot isostatically pressed zirconolite samples were produced by HIPing in 316 stainless steel tubes at a temperature of 1250 °C and overpressure of 100 MPa for four hours. To ensure a dense, HIPed product, $CaCO_3$ was replaced by $CaTiO_3$ to avoid the generation of CO_2 caused by thermal decomposition.

Reacted pellets were ground into a fine powder and characterised by powder X-ray diffraction (XRD). XRD was performed using a Bruker D2 Phaser diffractometer utilising Cu Kα radiation, utilising a Ni foil Kβ filter and a point step of 0.02 from 5 – 70 ° 2θ.

The microstructures of synthesised zirconolites were characterised by scanning electron microscopy (SEM) in combination with energy dispersive X-ray spectroscopy (EDX) using a Hitachi TM3030 SEM equipped with a Bruker Quantax EDX. An accelerating voltage of

15 kV was used. EDX data were processed using Bruker Quantax software. Sectioned zirconolites were prepared for SEM analysis by mounting in cold setting resin and polishing with SiC papers and diamond suspension to an optical finish of 1µm, before carbon sputter coating.

Samples were prepared for TEM analysis by grinding synthesised ceramics in a pestle and mortar with isopropanol and pipetting the solution on a carbon holey lined Cu TEM grid. Electron diffraction analysis was undertaken using a FEI Tecnai T20 TEM, with patterns captured using a CCD camera.

Mass loss during synthesis was investigated by thermogravimetric analysis using a Netzsch TG449 F3 Jupiter. Samples were heated at a rate of 20 $^{o}Cmin^{-1}$ in an argon atmosphere up to a temperature of 1450 ^{o}C, and changes in mass recorded.

Materials were studied using X-ray absorption near edge spectroscopy (XANES) to determine the average oxidation state of Mo and Ce. Samples were measured at the Mo K-edge (20,000 eV) using a conventional XAS setup at beamline BL-27b, Photon Factory, High Energy Accelerator Research Organization, Japan [22] and beamline B18, Diamond Light Source, United Kingdom. Ce L-III edge XANES (5723 eV) were measured at beamline 6-BMM, National Synchrotron Light Source II, Brookhaven National Laboratory, USA. Samples were prepared for XAS analysis by homogenously mixing ground, reacted powders with polyethylene glycol and uniaxially pressing to form 13 mm or 10 mm diameter pellets of approximately one absorption length.

Mo K-edge XANES were measured in transmission. Incident (I_0) and transmitted (I_t) X-ray intensities were measured using ionisation chambers. Energy calibration was performed by measuring a Mo foil. XANES spectra were measured from 30 eV below the edge of interest to 250 eV above. A Si (111) double crystal monochromator was used to tune the energy of incident photons giving an energy resolution of ± 0.3 eV.

Ce L-III edge XANES were measured in fluorescence using a four element Si drift detector. Energy calibration was performed using a CeO_2 standard mounted in front of a reference ion chamber placed after the sample. XANES spectra were measured from 30 eV below the edge of interest to 250 eV above. A Si (111) double crystal monochromator was used to tune the energy of incident photons giving an energy resolution of ± 0.3 eV.

Data reduction and XANES analysis were performed using the program Athena [23,24]. The Mo edge position was determined to be the energy at $\mu = 0.8$ of the absorption spectrum to avoid interference from pre-edge features as described by Farges *et al* [23]. The average Mo oxidation state was determined by performing a linear regression of first derivative energies with respect to standards of known oxidation state- MoO_2 (Mo IV), Sr_2HoMoO_6 (Mo V) and MoO_3 (Mo VI).

Results and discussion

Cold uniaxially pressed zirconolites

Powder X-ray diffraction showed the resultant phase assemblage in all cases predominantly comprised of zirconolite and perovskite with the relative phase abundances dependant on processing atmosphere, temperature, composition and the initial Ca precursor, as shown in Figures 1 and 2. Formation of the perovskite phase was found to occur to a greater extent in samples sintered at lower temperatures than high temperatures. This is likely due to the refractory nature of zirconium (IV) oxide, with higher reaction temperatures providing more favourable kinetics. Increasing the waste loading was found to result in increased formation of the perovskite phase and retention of zirconium oxide. The effects of the calcium precursor on the final phase assemblage can be observed in Figs. 1 and 2. Use of $CaTiO_3$ as a precursor was found to result in increased formation of the target zirconolite phase, however this influence was less pronounced at higher synthesis temperatures. The increased zirconolite yield onset by the $CaTiO_3$ precursor may indicate that zirconolite formation proceeds *via* the formation of a $CaTiO_3$ intermediate and subsequent diffusion of ZrO_2. A similar phenomenon was observed by Gilbert for zirconolites formed using the molten salt synthesis route [26]. The processing atmosphere was found to have a similar influence to the Ca precursor employed. When sintering under a reducing atmosphere (5 % H_2/N_2), lower synthesis temperatures produced a greater proportion of zirconolite than those samples sintered in an inert atmosphere (Ar). At higher temperatures this trend was found to reverse and sintering under an inert atmosphere produced a more favourable phase assemblage (i.e. a greater proportion of zirconolite) than sintering in a reducing atmosphere. Stennett *et al* (2017) successfully synthesised single phase molybdenum-doped zirconolites ($CaZrTi_{2-x}Mo_xO_7$, $x = 0.0 - 0.4$) by sintering at 1400 ºC, however the proposed mechanism of eventual Mo incorporation was *via* a $CaMoO_4$ intermediate, no evidence of which has been observed by XRD in the current study [27]. Considering the absence of XRD reflections indicative of the 4M polytype it was

concluded that the zirconolite produced was of the 2M polytype (the reflection of the 4M polytype at 2θ = 6.75 º was the most informative and diagnostic, given the overlap of 4M and ZrO_2 reflections at 2θ = 31.5 º [28]; a representative example can be found in the Supplementary Information). This was later confirmed using electron diffraction.

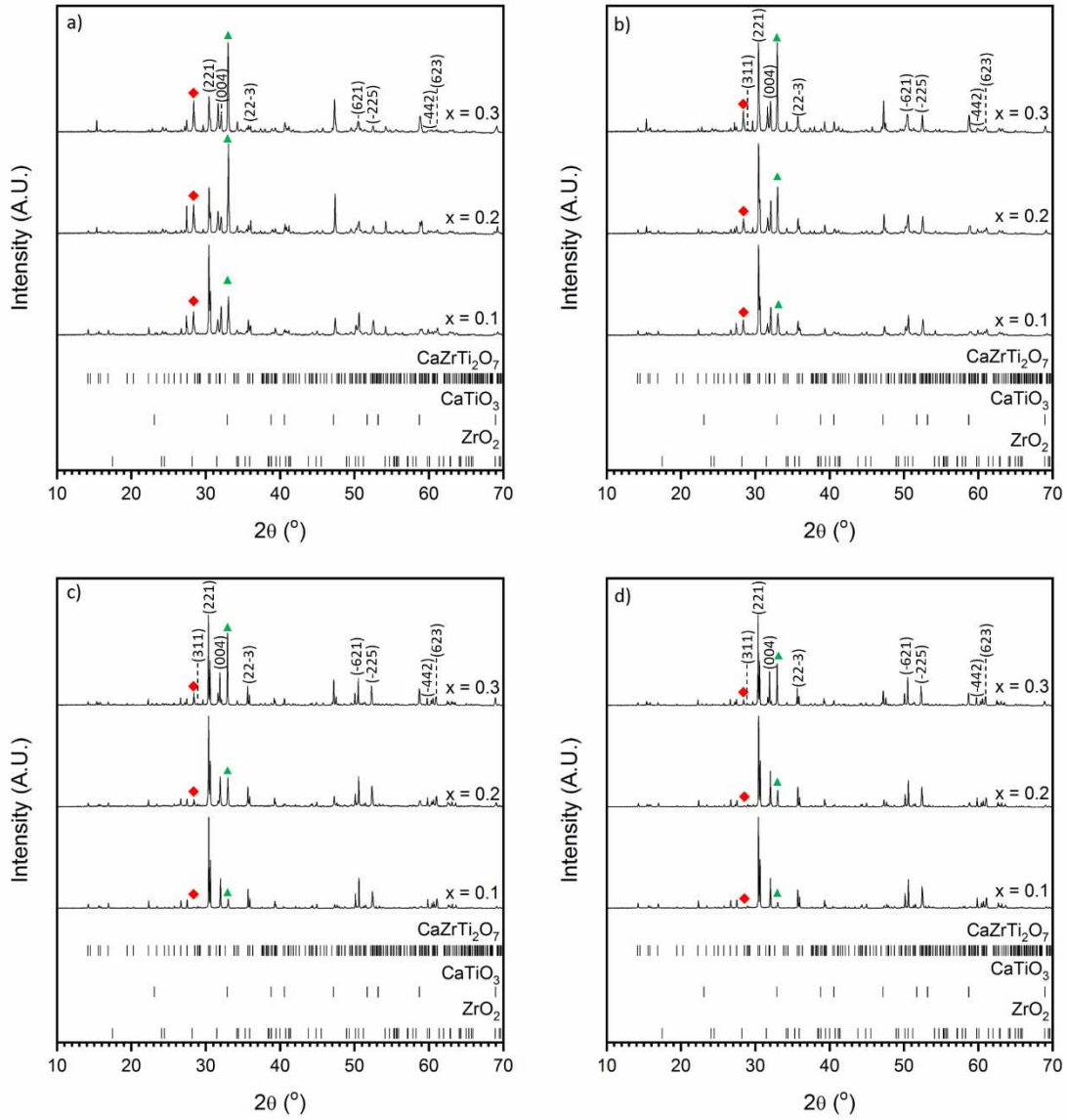

Figure 1: The effect of temperature, composition and Ca precursor on the formation of $Ca_{1-x/2}Zr_{1-x/2}Ce_xTi_{2-x}Mo_xO_{7\pm\delta}$ zirconolites (x = 0.1, 0.2 and 0.3) in an argon atmosphere. a) 1200 ºC, $CaCO_3$; b) 1200 ºC, $CaTiO_3$; c) 1400 ºC, $CaCO_3$ and d) 1400 ºC, $CaTiO_3$. Miller indices indicate major reflections for zirconolite 2M. Markers indicate major reflections for zirconia (red diamond) and perovskite (green triangle). Tick marks show allowed reflections for $CaZrTi_2O_7$-ICSD 72888, $CaTiO_3$- ICSD 94568 and ZrO_2- ICSD 41572.

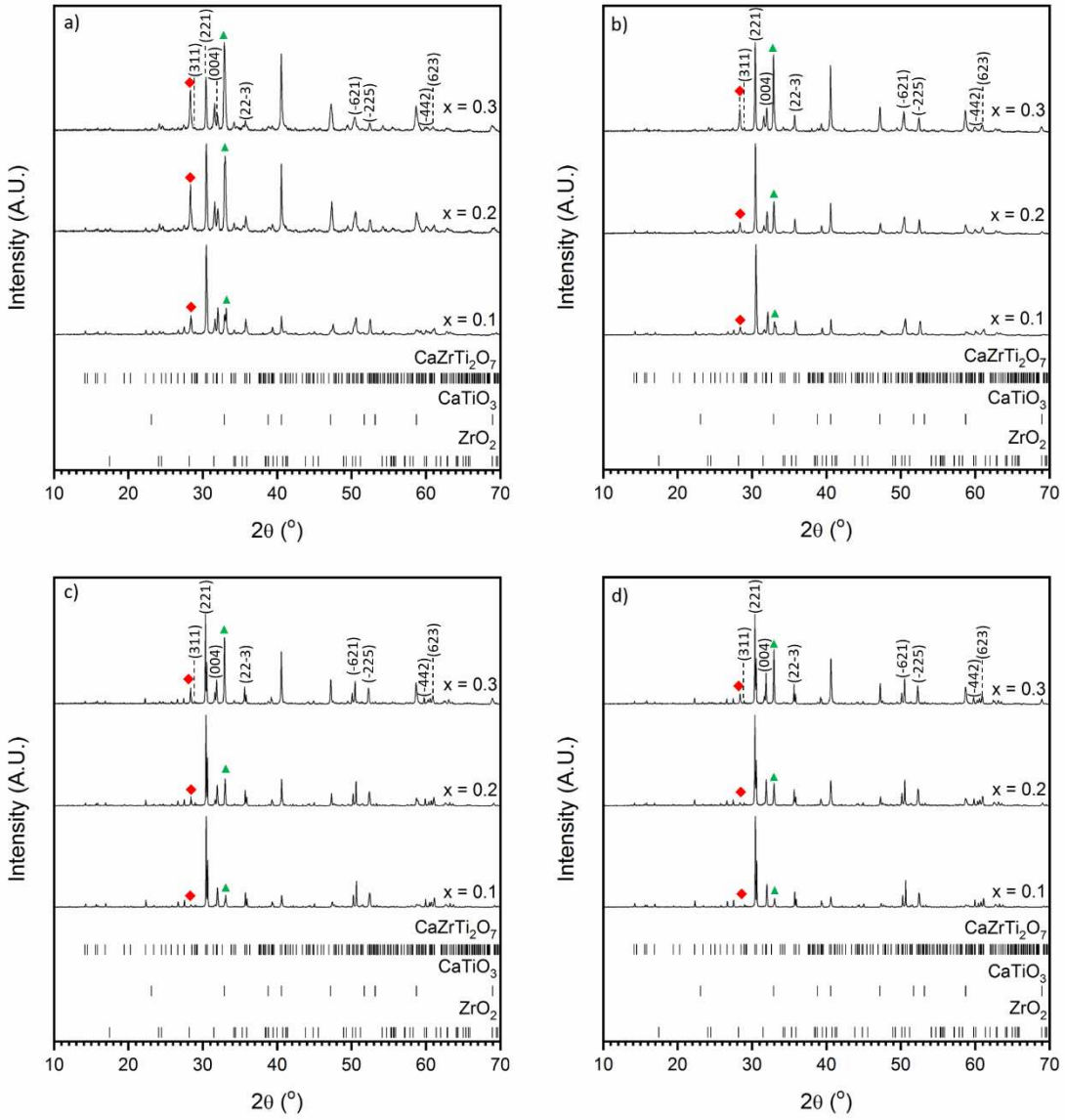

Figure 2: The effect of temperature, composition and Ca precursor on the formation of $Ca_{1-x/2}Zr_{1-x/2}Ce_xTi_{2-x}Mo_xO_{7\pm\delta}$ zirconolites (x = 0.1, 0.2 and 0.3) in a 5 % H_2/N_2 atmosphere. a) 1200 ºC, $CaCO_3$; b) 1200 ºC, $CaTiO_3$; c) 1400 ºC, $CaCO_3$ and d) 1400 ºC, $CaTiO_3$. Miller indices indicate major reflections for zirconolite 2M. Markers indicate major reflections for zirconia (red diamond) and perovskite (green triangle). Tick marks show allowed reflections for $CaZrTi_2O_7$- ICSD 72888, $CaTiO_3$- ICSD 94568 and ZrO_2- ICSD 41572.

Back scattered electron micrographs of the zirconolites sintered at 1200 °C are presented in Figure 3. Porosity can be observed in each sample as regions of dark contrast, suggesting this synthesis route led to poor sintering of the samples. Zirconolite formation was observed throughout each sample, with regions of $CaTiO_3$ and ZrO_2 also present, as was indicated by

#XRD. Notably, Mo metal was observed distributed throughout each sample. This phase was not identified using XRD. Mo-free zirconolites processed under comparable conditions (1400 ºC, 16 hr in Ar) by Vance *et al* (2002) [4] produced a product of comparably lower porosity. It is therefore hypothesised that the relatively poor sintering observed in this study is a result of Mo volatilisation.

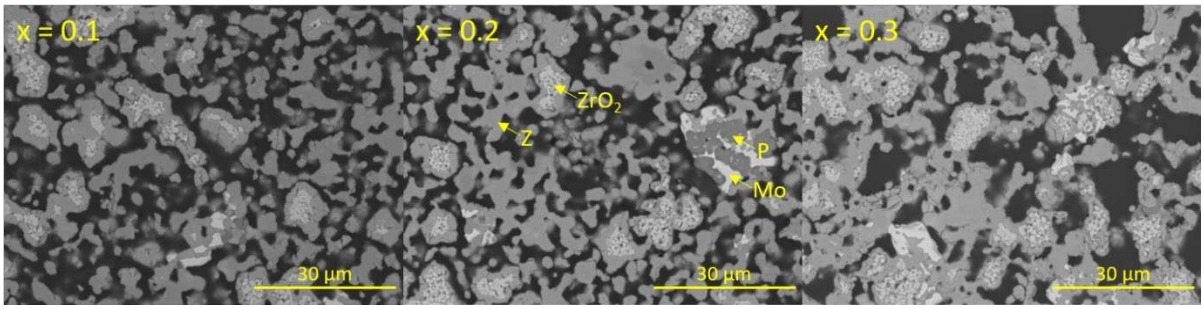

Figure 3: Representative electron micrographs of $Ca_{1-x/2}Zr_{1-x/2}Ce_xTi_{2-x}Mo_xO_{7\pm\delta}$ zirconolites sintered at 1200 ºC for 12 hours in argon (x = 0.1, 0.2 and 0.3). Z = zirconolite, Mo = molybdenum metal and P = perovskite.

The results of thermogravimetric analysis of zirconolites during synthesis in an Ar atmosphere are summarised in Table 1. The large initial mass loss observed in $CaCO_3$ containing precursors (T ≤ 950 ºC) was attributed to the decomposition of the carbonate and release of CO_2. Increasing substitution of CeO_2 for $CaCO_3$ and ZrO_2 was found to result in decreased weight loss and is therefore consistent with decomposition of $CaCO_3$, see Table 1. A second weight loss event was evident at temperatures > 950 ºC; this weight loss increased progressively with increasing Ce and Mo substitution and is believed to be a consequence of Mo volatilisation. Assuming that the high temperature mass loss was due to Mo volatilisation, the proportion of the initial Mo inventory lost decreased from 12.45 to 8.35 % when substitution was increased from 0.1 to 0.3 f.u.. Repetition of these analyses using $CaTiO_3$ precursors found that, as expected, mass loss was greatly reduced by eliminating the thermal decomposition of $CaCO_3$. The use of $CaTiO_3$ precursors was further observed to result in a decrease in the mass loss observed during the high temperature phase of the heat treatment (above 950 ºC). Unlike the results observed for zirconolites produced using $CaCO_3$, the proportion of the Mo inventory lost by volatilisation did not follow a decreasing trend but was instead observed to vary between 1.10-1.90 %.

Table 1: Mass losses during thermogravimetric analysis of $Ca_{1-x/2}Zr_{1-x/2}Ce_xTi_{2-x}Mo_xO_{7\pm\delta}$ zirconolites (%, ± 0.05 %).

x	Ca precursor	Mass loss 1 (< 950 ºC)	Mass loss 2 (> 950 ºC)	Estimated Mo loss
0.1	$CaCO_3$	10.67	0.34	12.45
0.2	$CaCO_3$	9.20	0.54	10.23
0.3	$CaCO_3$	8.10	0.64	8.35
0.1	$CaTiO_3$	0.43	0.03	1.10
0.2	$CaTiO_3$	0.61	0.10	1.90
0.3	$CaTiO_3$	0.70	0.11	1.44

Hot isostatically pressed zirconolites

A suite of samples was also prepared by hot isostatic pressing (HIPing). During HIPing, the samples were hermetically sealed within stainless steel tubing, thus eliminating the problem of Mo volatility. Figure 4 shows the resultant powder X-ray diffraction profiles of HIPed zirconolites and Figure 5 shows representative backscattered electron micrographs of their microstructures. The observed phase assemblages were highly similar to that of cold uniaxially pressed samples (CUPed), with increasing waste loading resulting in increased abundance of the perovskite phase. Considering the results observed for CUPed zirconolites, an increased processing temperature would likely result in reduced production of the perovskite phase and increased formation of zirconolite, this would require processing in an alternative can material to the 316 stainless steel used e.g. Ni. The resultant consolidated zirconolites showed markedly less porosity and improved sintering compared to those produced by cold pressing and sintering, as can be seen in Figure 5.

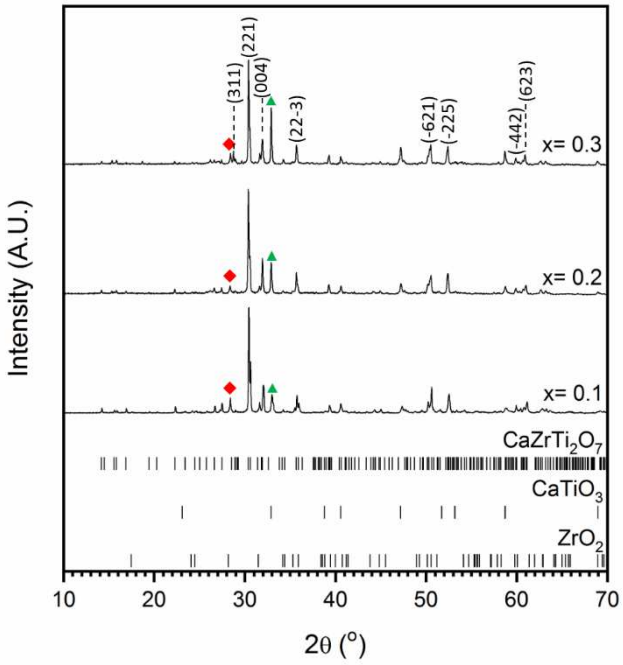

Figure 4: X-ray diffraction profiles of HIPed $Ca_{1-x/2}Zr_{1-x/2}Ce_xTi_{2-x}Mo_xO_{7\pm\delta}$ zirconolites (x = 0.1, 0.2 and 0.3). Miller indices indicate major reflections for zirconolite. Markers indicate major reflections for zirconia (red diamond) and perovskite (green triangle). Tick marks show allowed reflections for $CaZrTi_2O_7$- ICSD 72888, $CaTiO_3$- ICSD 94568 and ZrO_2 - ICSD 41572.

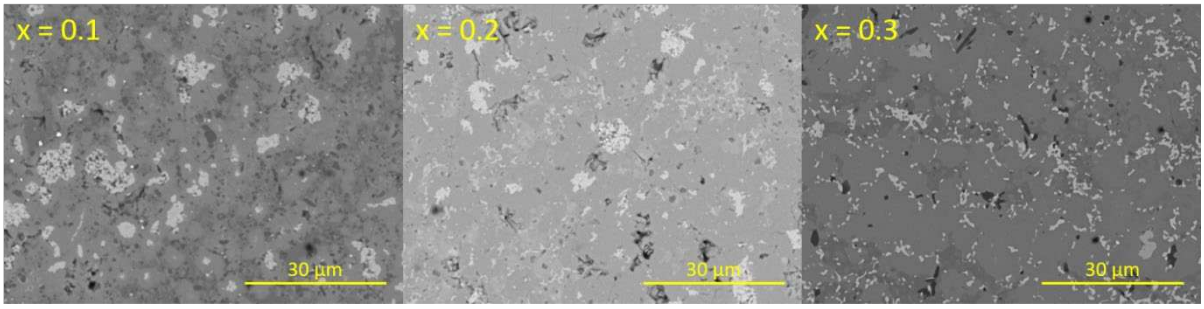

Figure 5: Representative backscattered electron micrographs of HIPed zirconolite formulations.

Study of elemental distribution by SEM-EDX (Figure 6, Tables 2 and 3) confirmed the formation of the $CaTiO_3$ phase and retention of ZrO_2. Mo was found to partition to both the zirconolite and perovskite phases and was also present throughout the sample as metallic Mo inclusions (bright contrast). The presence of reduced metallic Mo is similar to observations from previous studies of Tc incorporation into Synroc and rutile [29,30]. Ce was incorporated into the target zirconolite phase and the secondary perovskite phase as can be seen in Tables 2 and 3,

a similar phenomenon has been observed for the substitution of Nd^{3+} and Sm^{3+} by Jafar *et al* (2014) [31,32]. The partitioning of Ce to the perovskite phase could prove problematic in a final wasteform as, despite its relatively high tolerance to α-recoil damage, perovskite has proven to be less durable than other host phases, i.e. zirconolite[8,33]. This highlights the importance of optimising processing conditions and target stoichiometry to control the produced crystal chemistry. It is hypothesised that the apparent excess of positive charge in both the zirconolite and perovskite phases is offset by either the presence of cation vacancies, as suggested by Begg *et al* (1998) [34], or the reduction of Ti.

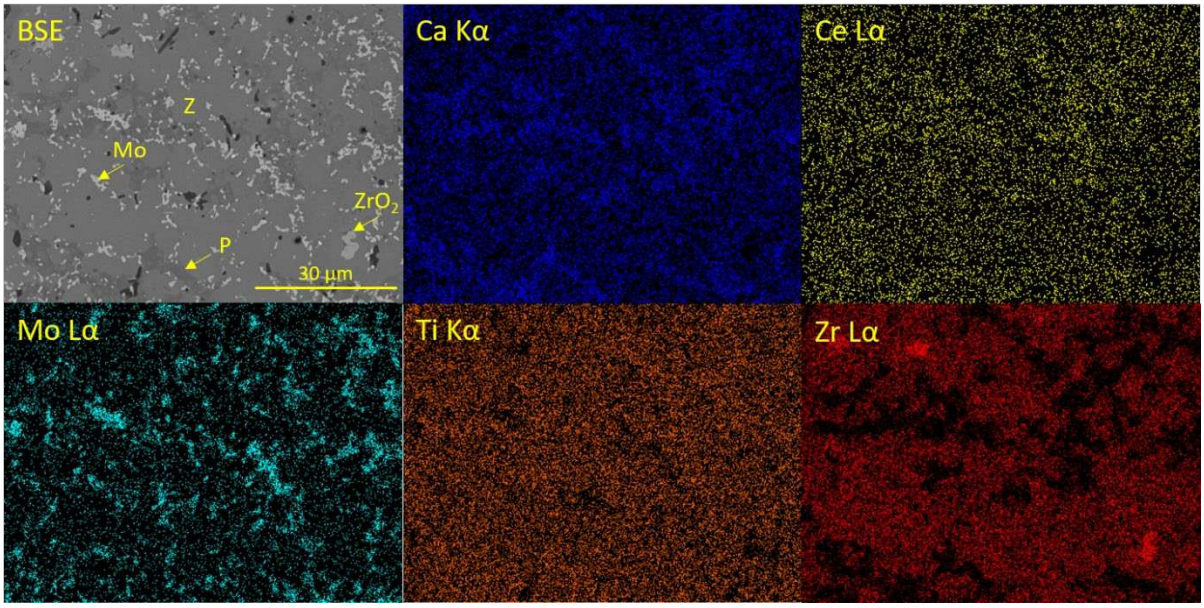

Figure 6: Elemental partitioning of HIPed $(Ca_{0.85}Ce_{0.15})(Zr_{0.85}Ce_{0.15})Ti_{1.7}Mo_{0.3}O_{7\pm\delta}$ zirconolite. Z = zirconolite, Mo = molybdenum metal and P = perovskite.

Table 2: Comparison of nominal composition and determined average composition synthesised by hot isostatic pressing.

	Cation stoichiometry (f.u.)				
Target composition	Ca	Zr	Ce	Ti	Mo
$(Ca_{0.95}Ce_{0.05})(Zr_{0.95}Ce_{0.05})Ti_{1.9}Mo_{0.1}O_7$	0.98 ± 0.08	0.89 ± 0.26	0.05 ± 0.02	1.95 ± 0.18	0.05 ± 0.02
$(Ca_{0.9}Ce_{0.1})(Zr_{0.9}Ce_{0.1})Ti_{1.8}Mo_{0.2}O_7$	1.02 ± 0.09	1.06 ± 0.12	0.08 ± 0.02	1.92 ± 0.12	0.08 ± 0.04
$(Ca_{0.85}Ce_{0.15})(Zr_{0.85}Ce_{0.15})Ti_{1.7}Mo_{0.3}O_7$	1.03 ± 0.07	1.12 ± 0.13	0.18 ± 0.06	1.85 ± 0.18	0.15 ± 0.03

Table 3: Determined average composition of perovskite phase in hot isostatically pressed $Ca_{1-x/2}Zr_{1-x/2}Ce_xTi_{2-x}Mo_xO_{7\pm\delta}$ zirconolites.

	Cation stoichiometry (f.u.)				
x	Ca	Zr	Ce	Ti	Mo
0.1	0.61 ± 0.03	0.09 ± 0.01	0.04 ± 0.01	1.00 ± 0.03	0.03 ± 0.01
0.2	0.67 ± 0.02	0.10 ± 0.01	0.17 ± 0.02	1.00 ± 0.03	0.05 ± 0.01
0.3	0.62 ± 0.03	0.08 ± 0.01	0.21 ± 0.01	1.00 ± 0.05	0.04 ± 0.01

Transmission electron microscopy (TEM)

Electron diffraction patterns of synthesised zirconolites were acquired to confirm the zirconolite polytype formed. In agreement with XRD results, electron diffraction patterns were found to index to the zirconolite 2M structure. The formation of the 4M polytype was not evident at the levels of substitution studied in this investigation. It remains possible that increased substitution on the A-site would lead to a change in symmetry, as observed by Vance *et al* (2002)[4].

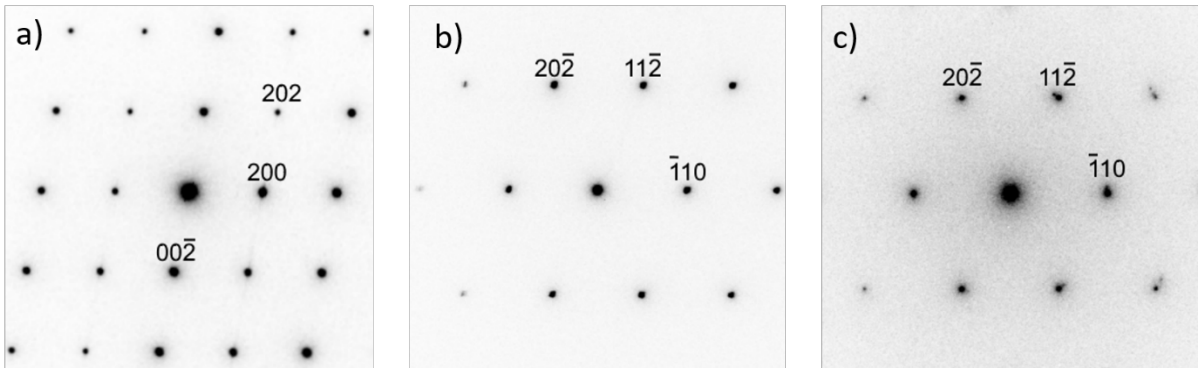

Figure 7: Zone axis electron diffraction patterns of $(Ca_{0.9}Ce_{0.1})(Zr_{0.9}Ce_{0.1})Ti_{1.8}Mo_{0.2}O_{7\pm\delta}$ synthesised under different processing conditions: a) HIP [010], b) Argon atmosphere [111] and c) 5 % H_2/N_2 atmosphere [111]. Indexed in the *C12/c1* space group.

X-ray absorption spectroscopy (XAS)

Mo compounds exhibit a pre-edge feature ~ 20-30 eV before the main absorption edge. The pre-edge feature is related to electronic transitions from 1s to 4d states for Mo in addition to quadrupolar 1s to 4d and dipolar 1s to 2p transitions to Mo or O nearest neighbours [25]. The intensity of the pre-edge feature increases as the 4d states become less occupied, hence the pre-edge feature is especially intense for Mo (VI) compounds when Mo is in a non-centrosymmetric site. The pre-edge feature of Mo (IV) or Mo (V) compounds are difficult to resolve and often appear as a shoulder on the main absorption edge [25]. The edge position itself has been shown to follow a linear trend with the oxidation state of Mo by Farges *et al* [25]. Mo speciation was determined by XAS and linear regression with respect to standards, see Figure 8 and 9. Results are summarised in Table 4.

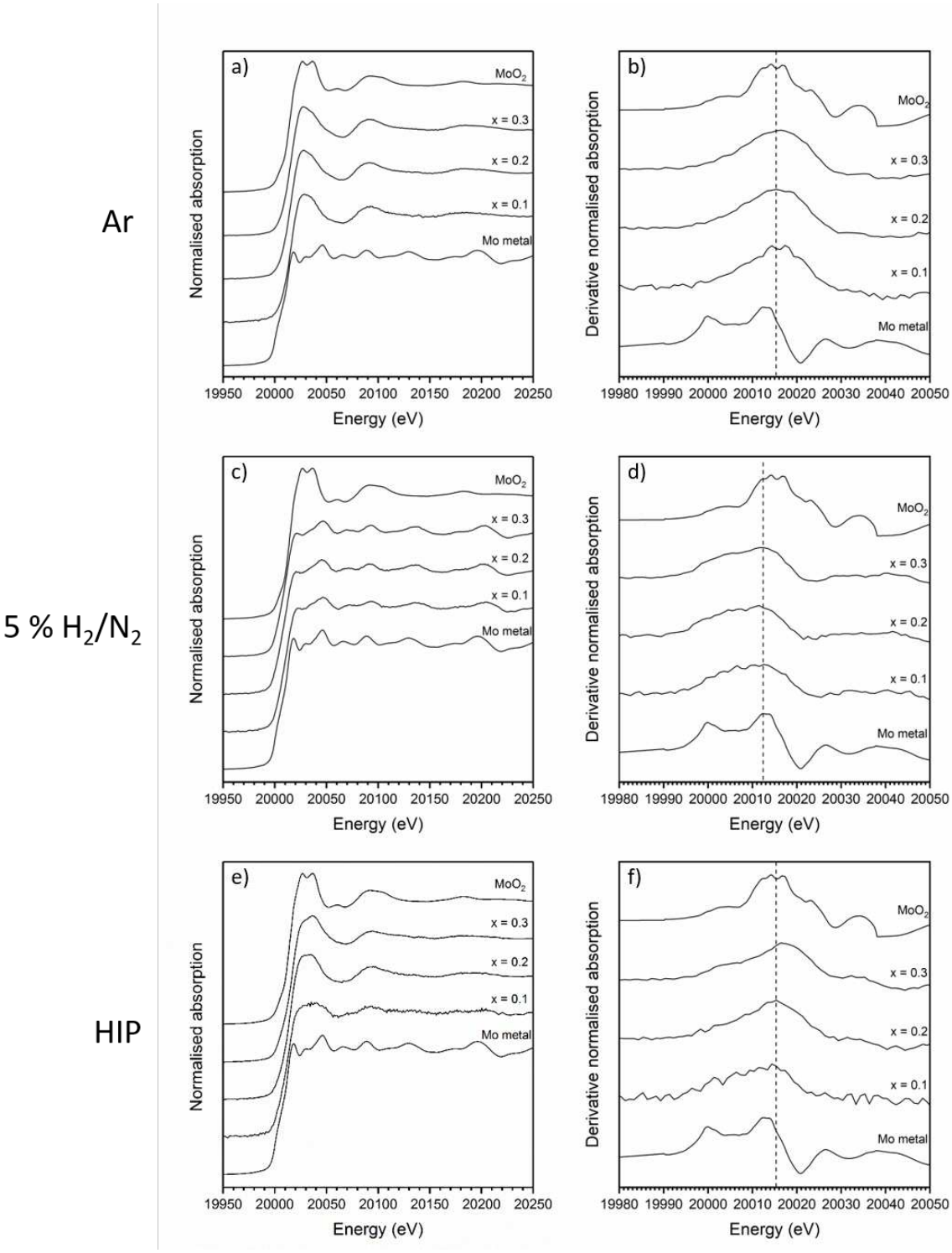

Figure 8: Mo K-edge XANES and derivative XANES of $Ca_{1-x/2}Zr_{1-x/2}Ce_xTi_{2-x}Mo_xO_{7\pm\delta}$ zirconolites synthesised in Ar and 5 % H_2/N_2 atmospheres or consolidated by HIP: a) Ar XANES; b) Ar derivative XANES; c) 5% H_2/N_2 XANES; d) 5 % H_2/N_2 derivative XANES; e) HIP XANES and f) HIP derivative XANES.

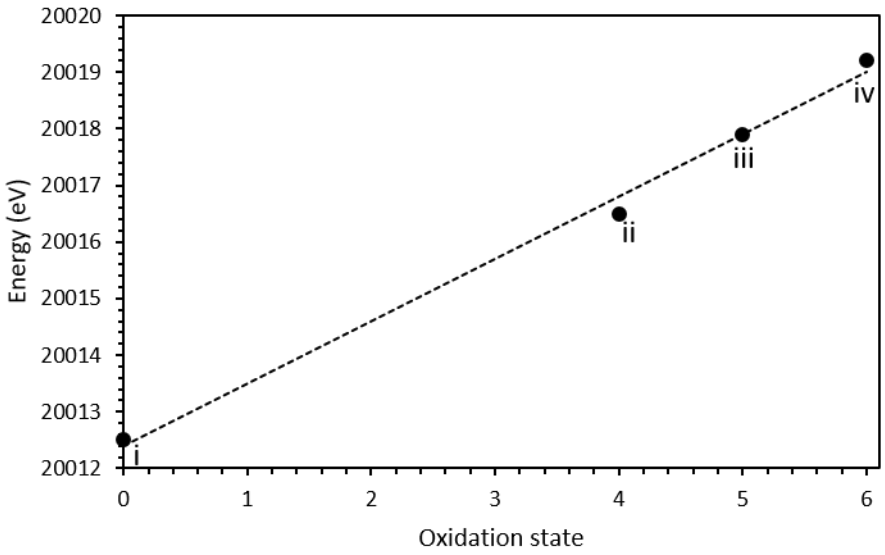

Figure 9: E_0 values of Mo standards i) Mo metal, ii) MoO_2, iii) Sr_2HoMoO_6 and iv) MoO_3. Line of best fit used to determine oxidation state of zirconolite samples by linear regression.

Table 4: Average Mo oxidation state of synthesised zirconolites as determined by linear regression with respect to standards.

Sample no.	Nominal composition	Atmosphere	E_0 (eV, ± 0.3)	Mean OS (±0.2)
1	$(Ca_{0.95}Ce_{0.05})(Zr_{0.95}Ce_{0.05})Ti_{1.9}Mo_{0.1}O_7$	Ar	20017.3	4.5
2	$(Ca_{0.9}Ce_{0.1})(Zr_{0.9}Ce_{0.1})Ti_{1.8}Mo_{0.2}O_7$	Ar	20016.4	3.6
3	$(Ca_{0.85}Ce_{0.15})(Zr_{0.85}Ce_{0.15})Ti_{1.7}Mo_{0.3}O_7$	Ar	20017.3	4.5
4	$(Ca_{0.95}Ce_{0.05})(Zr_{0.95}Ce_{0.05})Ti_{1.9}Mo_{0.1}O_7$	5 % H_2/N_2	20014.4	1.8
5	$(Ca_{0.9}Ce_{0.1})(Zr_{0.9}Ce_{0.1})Ti_{1.8}Mo_{0.2}O_7$	5 % H_2/N_2	20013.7	1.2
6	$(Ca_{0.85}Ce_{0.15})(Zr_{0.85}Ce_{0.15})Ti_{1.7}Mo_{0.3}O_7$	5 % H_2/N_2	20014.2	1.6
7	$(Ca_{0.95}Ce_{0.05})(Zr_{0.95}Ce_{0.05})Ti_{1.9}Mo_{0.1}O_7$	HIP	20015.7	3.0
8	$(Ca_{0.9}Ce_{0.1})(Zr_{0.9}Ce_{0.1})Ti_{1.8}Mo_{0.2}O_7$	HIP	20016.7	3.9
9	$(Ca_{0.85}Ce_{0.15})(Zr_{0.85}Ce_{0.15})Ti_{1.7}Mo_{0.3}O_7$	HIP	20018.4	5.5

Processing conditions were found to have a strong influence on Mo speciation. As can be seen in Figure 8, samples sintered in Ar were found to have edge positions and post-edge features

typical of Mo (IV), whereas the XANES features of samples sintered in 5% H_2/N_2 were found to be more similar to Mo metal. As Tc is more readily reduced to the metal form than Mo [35], it is likely that similar behaviour would be observed in samples with Tc. Samples prepared by HIP were found to have edge positions and post-edge features that indicated a mixture of metallic Mo and Mo (IV) in agreement with SEM investigation. With increasing substitution of Mo for Ti, it was noted that the edge position progressively shifted to higher energies. This may be attributed to the incorporation and stabilisation of higher Mo oxidation states in the perovskite phase [36], the proportion of which also increases with increasing Mo substitution, as shown in Figure 4. Although Mo was added as Mo (IV), it is possible the Mo was oxidised by redox coupling with either Ce or Ti, with the former more likely.

The absence of a strong pre-edge feature in the measured spectra indicates that any Mo incorporated is unlikely to be Mo (VI) and more likely Mo (IV/V). The results of Ce XANES analysis, presented in Figure 10, support the hypothesis of redox coupling as Ce is present in the Ce (III) oxidation state regardless of processing atmosphere.

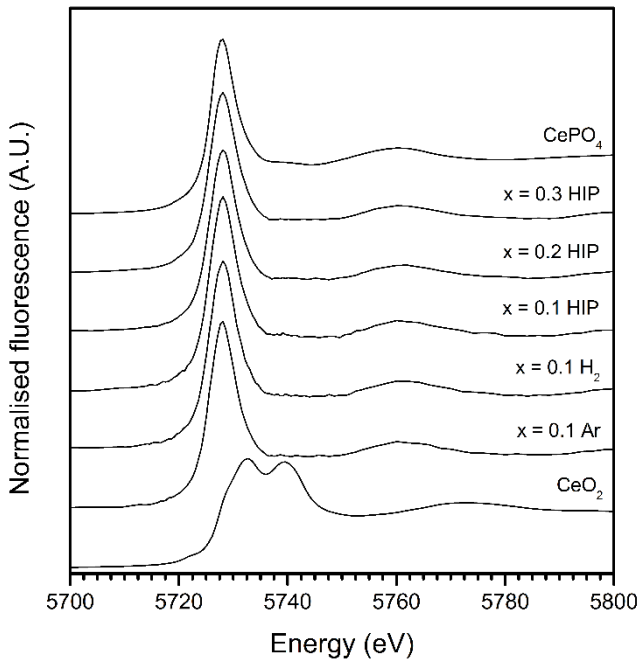

Figure 10: Ce L-III edge XANES of standards $CePO_4$ (Ce (III)), CeO_2 (Ce (IV)) and representative $Ca_{1-x/2}Zr_{1-x/2}Ce_xTi_{2-x}Mo_xO_{7\pm\delta}$ zirconolites synthesised in Ar and 5 % H_2/N_2 atmospheres or consolidated by HIP.

Conclusions

Target zirconolite compositions were synthesised under Ar, 5% H_2/N_2 and also by hot isostatic pressing. Zirconolite was formed in all cases with accompanying accessory phases. Zirconolite yield was found to be affected by processing atmosphere, temperature, composition and the initial Ca precursor used. Using $CaTiO_3$ as the Ca precursor was found to improve the final phase assemblage, i.e. a greater yield of zirconolite was formed, and Mo volatilisation was reduced. Achieving dense materials by traditional CUPing methods proved difficult as high temperature treatment exacerbated the problems of Mo volatilisation but sintering at lower temperatures was found to result in greatly decreased yields of zirconolites. HIPing was found to yield the highest density product and, with optimisation of the can material and redox conditions, would provide the best route for the co-immobilisation of Tc and TRUs in a zirconolite matrix. Ce was observed in both the target zirconolite phase and secondary perovskite phase, highlighting the importance of achieving the full reaction of precursors and the elimination of secondary phases. The partitioning behaviour of Mo was found to vary with processing atmosphere, whereas Ce was found to be universally present in the reduced Ce (III) oxidation state. When processed under Ar, Mo was found to remain in the Mo (IV) oxidation state and was partitioned to the zirconolite phase. Processing under 5% H_2/N_2 was found to result in Mo being reduced to Mo metal and encapsulated. Hot isostatic pressing of zirconolite batches yielded a mixture Mo metal, Mo (IV) and higher Mo oxidation states. It is hypothesised that the higher Mo oxidation states are stabilised by incorporation into the secondary perovskite phase.

Acknowledgements

DJB and SML are funded by the Engineering, Physical Sciences Research Council *via* the Nuclear FiRST Doctoral Training Centre (Grant EP/G037140/1) and Grant EP/M026566/1. NCH is grateful to the Royal Academy of Engineering and Nuclear Decommissioning Authority for funding. CLC wishes to acknowledge EPSRC for the award of an ECR Fellowship (EP/N017374/1). This research was performed in part at the MIDAS Facility, at the University of Sheffield, which was established with support from the Department of Energy and Climate Change. Use of the National Synchrotron Light Source II, Brookhaven National Laboratory, was supported by the U.S. Department of Energy, Office of Science, Office of Basic Energy Sciences, under Contract No. DE-AC02-98CH10886 and beamtime proposal

number 303200. We acknowledge Diamond Light Source for beamtime allocation at Beamline B18 under Proposal [SP17243].

Data Availability

The raw/processed data required to reproduce these findings cannot be shared at this time as the data also forms part of an ongoing study

References

1 I. W. Donald, *Waste Immobilization in Glass and Ceramic Based Hosts*, John Wiley & Sons Ltd., Chichester, 1st edn., 2010.

2 D. R. Olander, *J. Nucl. Mater.*, 2009, **389**, 1–28.

3 E. R. Vance, C. J. Ball, R. A. Day, K. L. Smith, M. G. Blackford, B. D. Begg and P. J. Angel, *J. Alloys Compd.*, 1994, **213**–**214**, 406–409.

4 E. R. Vance, G. R. Lumpkin, M. L. Carter, D. J. Cassidy, C. J. Ball, R. A. Day and B. D. Begg, *J. Am. Ceram. Soc.*, 2002, **59**, 1853–1859.

5 W. J. Weber, R. C. Ewing, C. R. A. Catlow, T. Diaz de la Rubia, L. W. Hobbs, C. Kinoshita, H. Matzke, A. T. Motta, M. Nastasi, E. K. H. Salje, E. R. Vance and S. J. Zinkle, *J. Mater. Res.*, 1998, **13**, 1434–1484.

6 E. R. Vance, C. J. Ball, M. G. Blackford, D. J. Cassidy and K. L. Smith, *J. Nucl. Mater.*, 1990, **175**, 58–66.

7 A. E. Ringwood, S. E. Kesson, N. G. Ware, W. Hibberson and A. Major, *Nature*, 1979, **278**, 219–223.

8 A. E. Ringwood, K. D. Reeve, D. M. Levins and E. J. Ramm, in *Radioactive Waste Forms for the Future*, eds. R. C. Ewing and W. Lutze, North Holland Physics Publishing, New York, 1988, pp. 233–335.

9 T. J. White, *Am. Mineral.*, 1984, **69**, 1156–1172.

10 T. J. White, R. L. Segall, J. L. Hutchinson and J. C. Barry, *Proceeds R. Soc. London A*, 1984, 343–358.

11 R. Gieré and P. Stille, *Energy, Waste and the Environment: a Geochemical Perspective*, 2004.

12 P. Bayliss, F. Mazzi, R. Munno and T. J. White, *Mineral. Mag.*, 1989, **53**, 565–569.

13 B. D. Begg, E. R. Vance and S. D. Conradson, *J. Alloys Compd.*, 1998, **271**–**273**, 221–226.

14 F. Mazzi and R. Munno, *Am. Mineral.*, 1983, **68**, 262–276.

15 G. R. Lumpkin, K. L. Smith, M. G. Blackford, R. Gieré and C. Terry Williams, *Micron*, 1994, **25**, 581–587.

16 R. Gieré, J. Malmström, E. Reusser, G. R. Lumpkin, M. Düggelin, D. Mathys, R. Guggenheim and D. Günther, *Mat. Res. Soc. Symp. Proc.*, 2001, **663**, 267–275.

17 P. J. McGlinn, T. Advocat, G. Leturcq, T. I. McLeod, Z. Aly and P. Yee, *Mat. Res. Soc. Symp. Proc.*, 2006, **932**, 3–9.

18 S. A. Luksic, B. J. Riley, M. Schweiger and P. Hrma, *J. Nucl. Mater.*, 2015, **466**, 526–538.

19 R. D. Shannon, *Acta Crystallogr.*, 1976, **32**, 751–767.

20 O. Muller, *J. Inorg. Nucl. Chem.*, 1964, **26**, 2075–2086.

21 T. Hartmann, A. J. Alaniz and D. J. Antonio, *Procedia Chem.*, 2012, **7**, 622–628.

22 H. Konishi, A. Yokoya, H. Shiwaku, H. Motohashi, T. Makita, Y. Kashihara, S. Hashimoto, T. Harami, H. Maeta, H. Maezawa, S. Asaoka, N. Kanaya, K. Ito, N. Usami and K. Kobayashi, *Nucl. Instruments Methods Phys. Res. A*, 1996, **372**, 322–332.

23 B. Ravel and M. Newville, in *Journal of Synchrotron Radiation*, 2005, vol. 12, pp. 537–541.

24 B. Ravel and M. Newville, *Phys. Scr.*, 2005, 1007.

25 F. Farges, R. Siewert, G. E. J. Brown and A. Guesdon, *Can. Mineral.*, 2006, **44**, 731–753.

26 M. R. Gilbert, *Mater. Res. Soc. Symp. Proc.*, 2014, **1665**, 325–330.

27 M. C. Stennett, T.-H. Lee, D. J. Bailey, E. V Johnstone, J. Heo and N. C. Hyatt, *MRS Adv.*, 2017, **2**, 753–758.

28 M. Jafar, S. N. Achary, N. P. Salke, A. K. Sahu, R. Rao and A. K. Tyagi, *J. Nucl. Mater.*, 2016, **475**, 192–199.

29 K. P. Hart, E. R. Vance, R. A. Day, B. D. Begg, P. J. Angel and A. Jostsons, *Mat. Res. Soc. Symp. Proc.*, 1996, **412**, 281–287.

30 E. R. Vance, K. P. Hart, M. L. Carter, M. J. Hambley, R. A. Day and B. D. Begg, *Mater. Res. Soc. Symp. Proc.*, 1998, **506**, 289–293.

31 M. Jafar, P. Sengupta, S. N. Achary and A. K. Tyagi, *J. Am. Ceram. Soc.*, 2014, **97**, 609–616.

32 M. Jafar, P. Sengupta, S. N. Achary and A. K. Tyagi, *J. Eur. Ceram. Soc.*, 2014, **34**, 4373–4381.

33 K. L. Smith, N. J. Zaluzec and G. R. Lumpkin, *Mater. Res. Soc. Symp. Proc.*, 1998, **506**, 931.

34 B. D. Begg, E. R. Vance and G. R. Lumpkin, *Mat. Res. Soc. Symp. Proc.*, 1998, **506**, 79–86.

35 H. Kleykamp, *J. Nucl. Mater.*, 1985, **131**, 221–246.

36 A. F. Fuentes, M. Garza-García, J. I. Escalante-García, G. Mendoza-Suárez, K. Boulahya and U. Amador, *J. Solid State Chem.*, 2003, **175**, 299–305.

A new approach to the immobilisation of technetium and transuranics: co-disposal in a zirconolite ceramic matrix- Supplementary Information

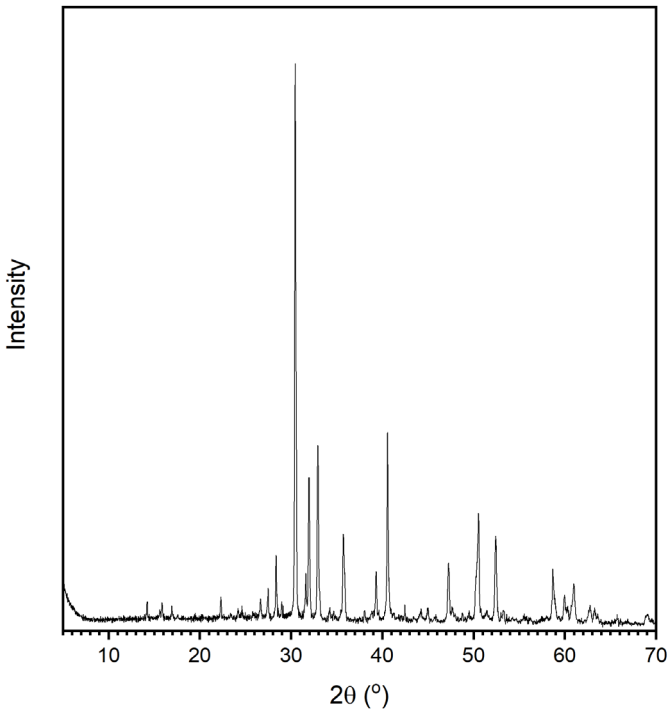

SF1: X-ray diffraction profile of $(Ca_{0.9}Ce_{0.1})(Zr_{0.9}Ce_{0.1})Ti_{1.8}Mo_{0.2}O_7$ sintered at 1250 ºC in 5% H_2/N_2 atmosphere. Peaks diagnostic of 4M polytype at 6.75 º 2θ are absent.

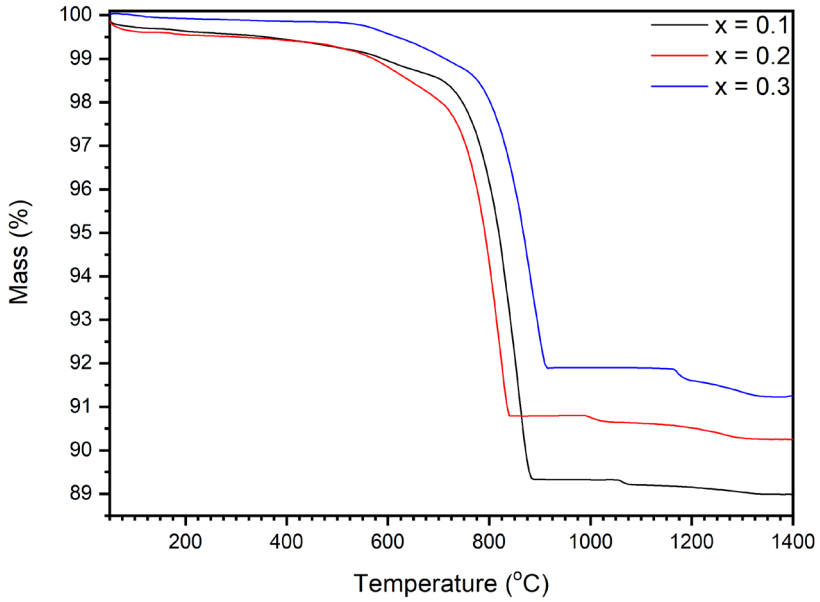

SF2: Results of thermogravimetric analysis of $Ca_{1-x/2}Zr_{1-x/2}Ce_xTi_{2-x}Mo_xO_{7\pm\delta}$ zirconolite batches with $CaCO_3$ precursor

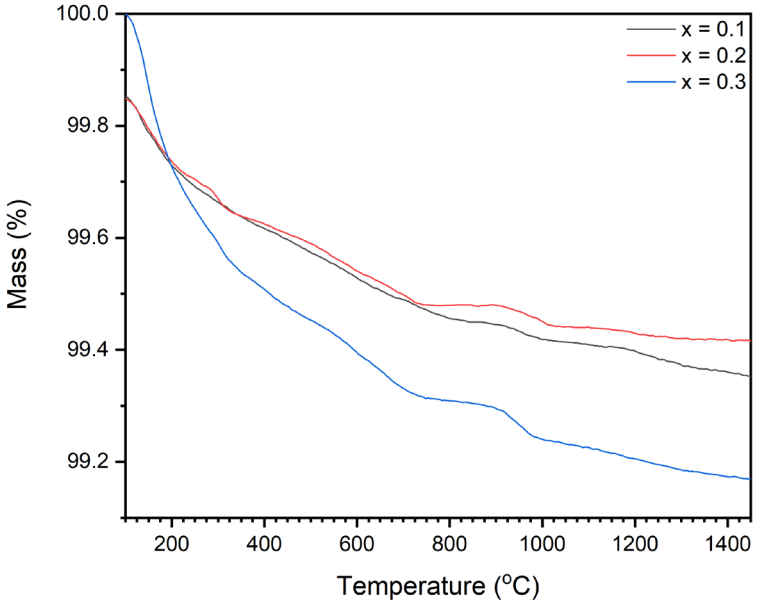

SF3: Results of thermogravimetric analysis of $Ca_{1-x/2}Zr_{1-x/2}Ce_xTi_{2-x}Mo_xO_{7\pm\delta}$ zirconolite batches with $CaTiO_3$ precursor